Proceedings of the 11th RSI International Conference on Robotics and Mechatronics (ICRoM 2023), Dec. 19-21, 2023, Tehran, Iran

Design and Fabrication of a Vision-based Tactile Sensor

Mohammad Amin Mirzaee
School of Mechanical Engineering
University of Tehran
Tehran, Iran
amin.mirzaee@ut.ac.ir

Ali Sadighi
School of Mechanical Engineering
University of Tehran
Tehran, Iran
asadighi@ut.ac.ir

***Abstract*— The sense of touch is an essential element for robotic arms in manipulating objects and their optimal interaction with the environment. Tactile sensors provide extensive quantitative and qualitative information about the contact between the sensor and the target object. With the advancements in machine vision and image processing, vision-based tactile sensors have been introduced as a more versatile sensing technology. This paper covers the steps of design, fabrication, and calibration of a vision-based tactile sensor. A brief introduction to optical simulation is presented and the convolutional neural networks model is used as the force estimation model for the simulation and experimental data. The fabricated sensor is capable of detecting normal-axis forces up to 5 newtons and tangential forces in two directions up to slip (approx. 1.4 times the applied normal force). The mean square error obtained for the built sensor is equal to 0.038 newtons in the vertical axis and 0.0033 and 0.0039 newtons in the two tangential axes on all the experimental data.**

Keywords—Tactile sensing, optical simulation, force estimation, convolutional neural networks (CNN)

I. INTRODUCTION

The sense of touch in humans and robots plays an essential role in identifying and controlling objects [1]. To enhance the performance of robotic arms, whether in robotic prostheses or industrial arms, tactile sensors are required to give us similar information to human touch. By employing them, robots can improve their interaction and perception skills for a much safer and dexterous manipulation in the environment [2].

To incorporate tactile sensing in robots, several transduction mechanisms based on specific physics have been developed. For example, tactile sensors based on electrical impedance sensing [3], piezoelectric materials [4], magnetic [5], pneumatic [6], and optical [7] are among the most popular sensors. Most of the aforementioned sensors are limited to low-resolution sensing of the applied force, its dynamics, and contact point in different conditions [8].

Vision-based tactile sensors have overcome many of the limitations of previous sensor mechanisms and provide high-resolution information [9] about not only the force characteristics, but also texture, hardness, shape, and direction of the object. The comprehensiveness of vision-based tactile sensors makes it necessary to propose a detailed framework for their design-to-manufacturing process.

There are three main approaches for converting physical deformation of the elastomer material into optical signals in the image [10]: Light conductive plate [11], [12], reflective membrane [13], [14], and marker displacement [15], [16]. Using the marker displacement is the most popular method. Since the initial location of the points in the sensor is known, in addition to measuring the forces applied to the surface [17], [18] and the contact point of the object [19], [20], these sensors can measure the applied torque to the surface [9] and detect slip [16], [21], [22]. By combining the mechanism of markers and reflective layer, a new type of sensor was introduced having the capabilities of both types of sensors [16], [23].

Most of the built sensors, due to the simplicity of the manufacturing and testing process, have a flat contact surface that can only sense the forces applied from above. Johnson et al. [13] designed a flat tactile sensor called GelSight to detect the surface texture of objects using the mechanism of a reflective membrane. The sensor could measure surface details in the range of a few microns. Yuan et al. [16] used another version of the GelSight sensor by combining the marker mechanism with the reflective membrane to measure shear and slip. Algorithms were implemented by measuring the displacement vector of the markers in each frame.

The introduced sensors were designed based on trial-and-error approaches and there was not much prior information on the sensor output before the fabrication stage and only limited mechanical simulations using finite element methods and experimental tests were performed to check the hardness of the sensor's elastomer. Recently, there have been new attempts at the simulation of vision-based tactile sensors whether for simulating deformation of the elastomer or for the optical aspect of the sensor. Agarwal et al. [24] proposed a physics-based rendering method to simulate the optical domain of a previously designed GelSight [9]. To simulate the sensor, accurate light models and analysis of individual components were needed. The proposed physics-based rendering technique performed considerably better than similar optical simulators. Si et al [25] introduced the first simulation framework that incorporated marker motion field and optical simulation of the GelSight tactile sensors using a polynomial look-up table for the optical response and linear displacement relationship and superposition principle for simulating the elastomer deformation.

Research on the simulation of the tactile sensors is focused on regenerating the image of a previously-designed tactile sensor. So, the simulation results are mostly used in robotic grasp simulation after fabricating the sensor. In this research, we cover the simulation of the sensor in the design stage prior to fabrication. As such, we can estimate the fabricated sensor output in the early stage and make required adjustments to achieve desired performance. Fig. 1 illustrates the working principle of the proposed vision-based tactile sensor and its corresponding subsystems.

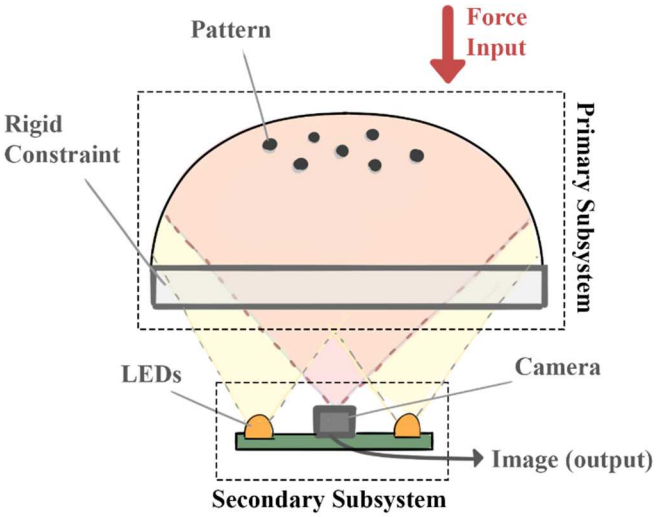

Fig. 1. The working principle of the vision-baed tactile sensor based on the marker displacement approach

The primary subsystem is a deformable elastomer on which the force is applied making the pattern deviate from its neutral state. The secondary subsystem comprises a small camera capturing images of the deformed pattern with a light source such as LEDs that would shed light on the pattern surface to increase the image quality and reduce background noise.

II. Sensor Design

In a vision-based tactile sensor, the camera and processor collect and manage contact surface data. Every aspect of the camera and embedded lenses has a direct impact on the sensor design phase. Factors such as depth of field (DOF), field of view (FOV), aspect ratio (AR), focal length, minimum focus distance (MFD), size, resolution, image sensor area, and pixel size must be evaluated at the initial design stage.

When choosing a compliant elastomer for the sensor, several considerations must be taken into account: optical transparency, hardness, stretchability, robustness, and fabrication complexity [9]. Typically, the sensor elastomer base should be soft enough to detect small contact forces. Nonetheless, sensors operating in high-load conditions require a stiffer elastomer base to ensure the elastomer is sensitive across its entire measurement range. For now, it was decided that the designed sensor would be able to measure normal force up to 5 newtons while maintaining a small strain level.

A. Camera Selection

In the current study, the camera has to capture acceptable-sized images (width and height) of relatively close objects to obtain a compact sensor configuration. Raspberry Pi Camera Module V2 was selected for its low cost, adjustable focus distance, and compatibility with processors such as Raspberry Pi and Nvidia Jetson Nano. One of the leading advantages of this camera module is its adjustable focus distance which facilitates sensor design optimization without increasing the height. To examine the Raspberry Pi Camera Module V2, a simplified test setup with an adjustable plane was 3D-printed to measure the MFD, DOF, and image area. The Raspberry Pi Camera Module V2's MFD could be adjusted by rotating the lens frame of the camera. There is a trade-off between the MFD and image area; therefore, by trial and error, the MFD was set to cover an acceptable image area while a desirable DOF of more than 1 mm was obtained. The final measured distance for the sensor's design is approximately 20 mm.

When the pattern distance from the camera is calculated, the design stage of the compliance and the sensor body structure could be started. It should be noted that the calculated pattern distance that the camera is set to be focused on in this stage is different from the actual pattern distance that should be considered for the sensor design. This difference is due to the multiple refractive indexes of the materials in front of the camera up to the pattern surface resulting in refraction. A Matlab code is scripted to compensate for the effect of intermediate layers. The glass distance to the camera is adjusted so as to get the best DOF while maintaining an adequate thickness for the elastomer. Eventually, the pattern is placed in the 23.5 mm from the camera to satisfy all the requirements.

B. Material selection and initial elastomer design

PDMS is selected for the compliant material in the current study because of the low drift of its properties over time with no significant change in physical dimensions and mechanical properties [26]. Regarding the design of the elastomer, it was determined to fabricate the compliance in two separate parts so that one of them functions as a white background for the pattern. Patterns could be designed in different shapes and forms. Fig. 2 illustrates the designed pattern which consists of 32 points on a square grid of 2 mm resolution.

The compliance design is an iterative task of geometry design and simulation. Considering the sensor specifications and assumptions, an initial geometry is designed. It is then simulated in COMSOL Multiphysics to evaluate the stress and strain level of the compliance to have a strain level of less than 20 percent (value averaged from articles [27], [28], [29]) that would maintain a relatively linear elastic behavior for PDMS. After some iterations, the optimal design is achieved, as illustrated in Fig. 3. Curvature at the center of the skin has a relatively higher radius letting the pattern be in focus while deforming.

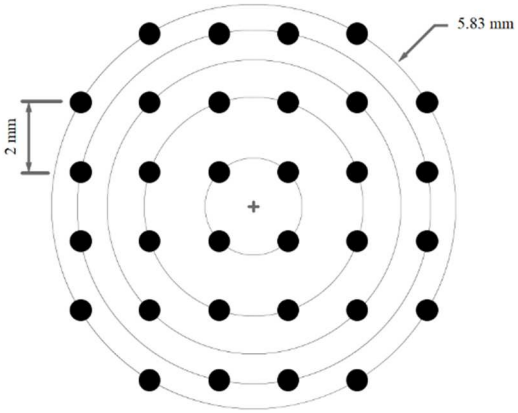

Fig. 2. Structure of the designed pattern

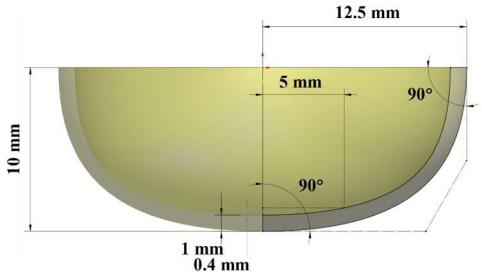

Fig. 3. Sketch of the deformable component. The 5 mm is the area captured in the image which corresponds to 0.4 difference in the depth

C. Simulation

The COMSOL Multiphysics software is used for simulating the sensor's subsystems. Accordingly, two of the software's module are used: "Solid Mechanics" and "Geometrical Optics."

1) Solid Mechanics

Solid Mechanics physics is used to simulate force application on PDMS compliance. PDMS is assumed to be a homogenous linear elastic domain to reduce the computational load of the simulation. The pattern is added on the middle surface of the PDMS body. Accordingly, for each dot in the designed pattern, sets of points with an outer radius of 0.3 mm are placed on the surface in a mesh-controlled mode so that all the points would be used in the meshing step of the PDMS. A block is imported into the simulation to apply force to the compliance. Stationary steps with a sweep parameter covering the normal and tangential force ranges are used.

2) Geometrical Optics

Geometrical Optics physics is used to model the camera. In Geometrical Optics physics, the path of light beams can be computed, and the output image is created by counting the number of beams that collide with a particular surface, known as the image sensor. The rays are emitted from every single point in the pattern (32 sets of 19 points according to the pattern design). The canonical ray groups with uniform density and cone angle of $\pi/100$ are released from every single point of the pattern to the camera diaphragm. The image sensor surface is meshed into equal-size squares to mimic the pixels in camera image sensors (considered 200 px × 200 px).

D. Simulation results

Fig. 5 shows the output of the simulation. It is observed that whether the force is applied to the compliance or not, the output images are relatively similar to each other. Another set of data is generated by subtracting the neutral image pixel values from that of all other images to illustrate the difference in each sample. This way, the corresponding data of the neutral image would become all-black pixels by subtracting equal values. However, as force is applied, the pixel values would change, showing the variations between the two images. In Fig. 6, it is shown that applying normal force to compliance would scatter the pattern dots from the center symmetrically. It is also observed that applying tangential forces to compliance would shift all the dots in the same direction. By changing the color map of the subtraction images, it is observed that there are two sets of pixel values in the images. Denoised subtraction data is obtained by thresholding the values in the noisy set.

A convolutional neural network model is used to estimate the normal and tangential force. The optimal model in terms of mean squared error (MSE) on the test (10%) and train data (90%) has the structure shown in Fig. 6. The model is trained for 500 epochs with a learning rate of 0.0001. MSE is considered as the loss function and the LeakyReLU activation function is applied to hidden layers.

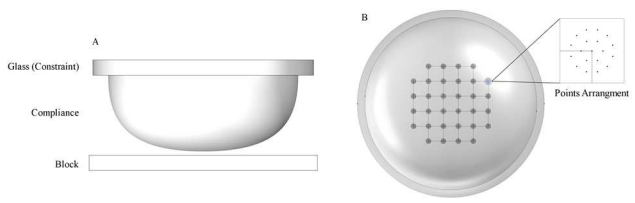

Fig. 4. COMSOL simulation imported geometries and the pattern

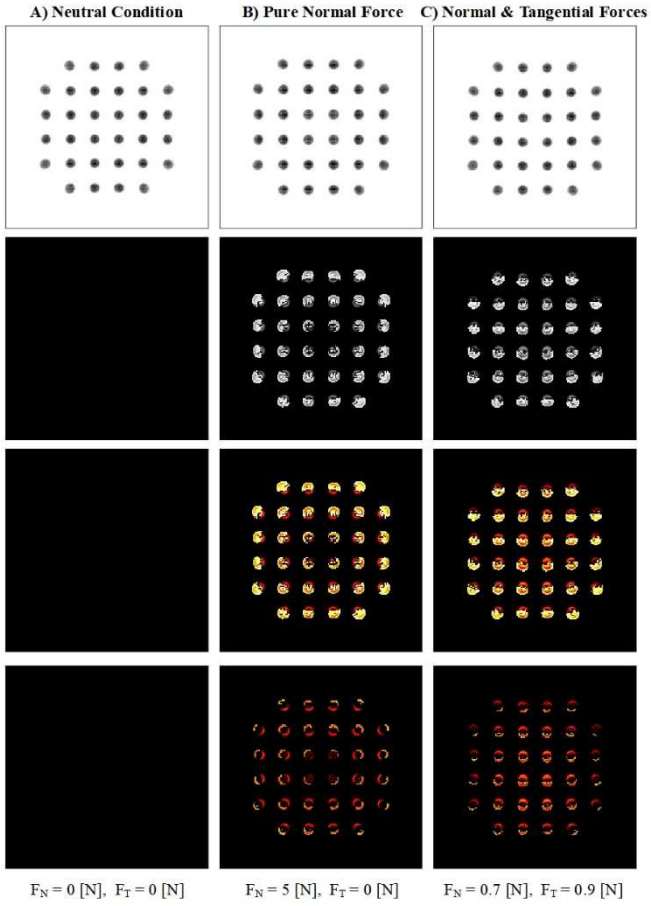

Fig. 5. Simulation results

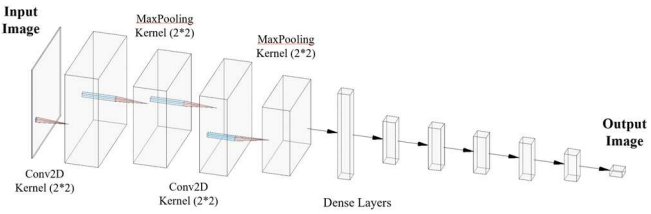

Fig. 6. Structure of the optimal model

The prediction performance of the model is shown in Fig. 7. It is observed that the normal force prediction performance of the model trained on the denoised data was significantly improved compared to the two other models. However, the raw data model showed a better estimation of the tangential-axis force. Altogether, comparing the performance of the models in terms of MAE and MSE, the denoised-data model's overall prediction performance on normal and tangential forces is more desirable. Therefore, it is suggested to use the denoised data not only for better predictions but also for less computational complexities.

E. Detailed Design

The initial design stage and simulation have clarified the working principle of the proposed vision-based sensor. The cross section of the sensor is illustrated in Fig. 8. Except for the aluminum part, all other components are designed to be made of 3D-printed polycarbonate for its hardness and high strength. The 3D-printed parts' tolerances are set for tight-fitted assembly to reduce the risk of disorientation.

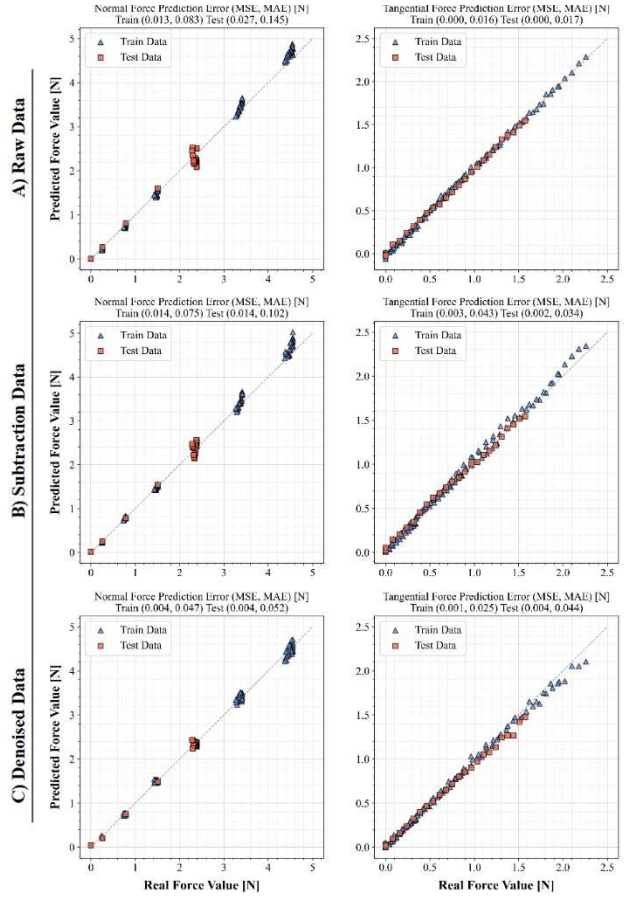

Fig. 7. Prediction performance of the CNN model on the simulation data

III. Fabrication

The fabrication process of the elastomer is shown in Fig. 9. Aluminum molds are designed to cast PDMS compliance material into the desired shape in two steps. Firstly, the white-pigmented PDMS is cast so that the dot pattern could be drawn into the inner surface of it after using a primer liquid (making the black glue better attach to the PDMS surface). Then, the transparent PDMS is poured into the mold and cured to have it attached to a circular plexiglass.

The assembly steps for the fabricated sensor are shown in Fig. 10. The sensor is connected to the Raspberry Pi development board to capture images of the pattern with 30 frames per second.

IV. Data Acquisition

A closed-loop force application system was developed in [5]. The same system is used in this study to collect data from the sensor. Fig. 11 illustrates the mechanism and details of the force application system. Two voice coil actuators are employed to apply force in the normal and tangential axes. Two load cells are attached to these two voice coils to measure the applied force and provide feedback for closed-loop control. A plexiglass block is used as the end-effector similar to the simulation stage. The Raspberry Pi and STM32F429I-DISC1development boards sample data synchronously with STM32F429I-DISC1 receiving external interrupt in each frame. The sensor is rotated on the base to collect data on the two orthogonal tangential axes.

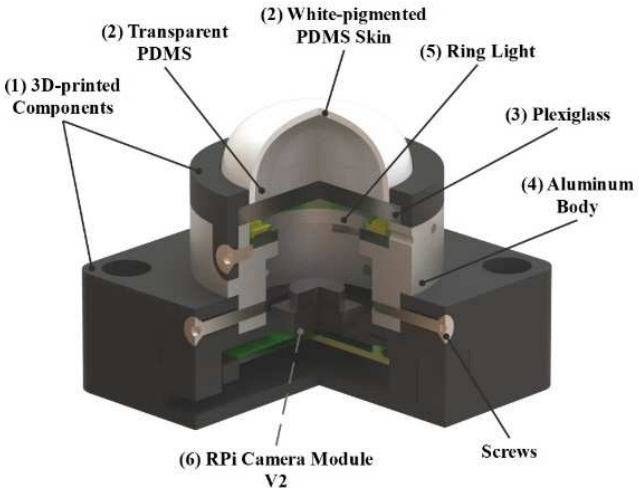

Fig. 8. Cross-section view of the proposed tactile sensor

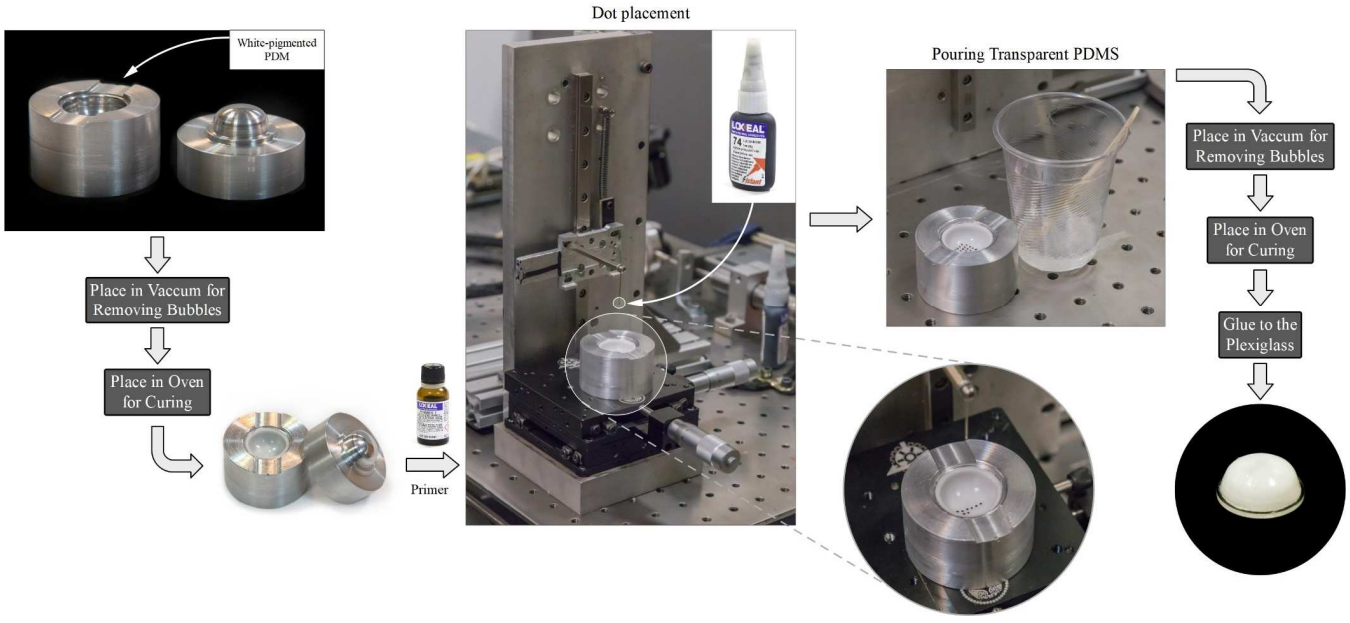

Fig. 9. Fabrication steps of the deformable component from PDMS

Fig. 10. Assembly steps of the fabricated sensor

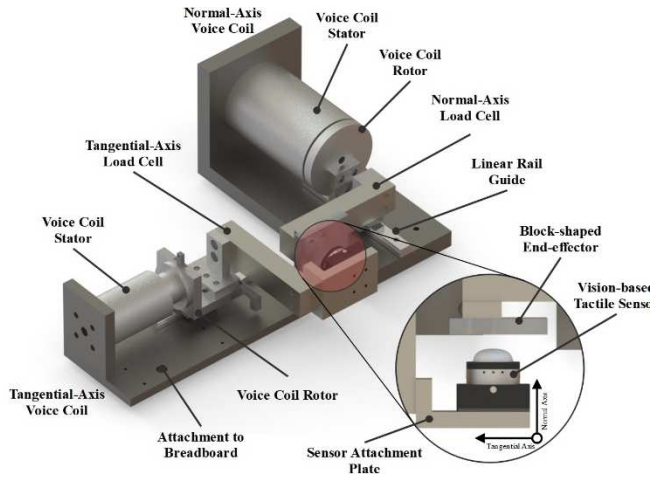

Fig. 11. Force application system for sensor data acquisition

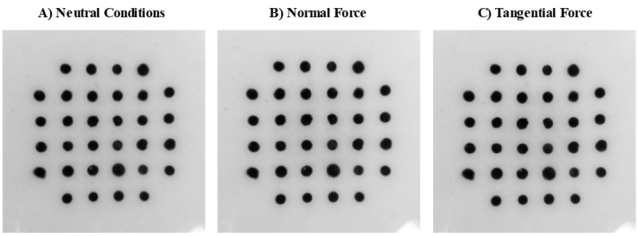

Fig. 12. Sample image of the sensor in different force conditions

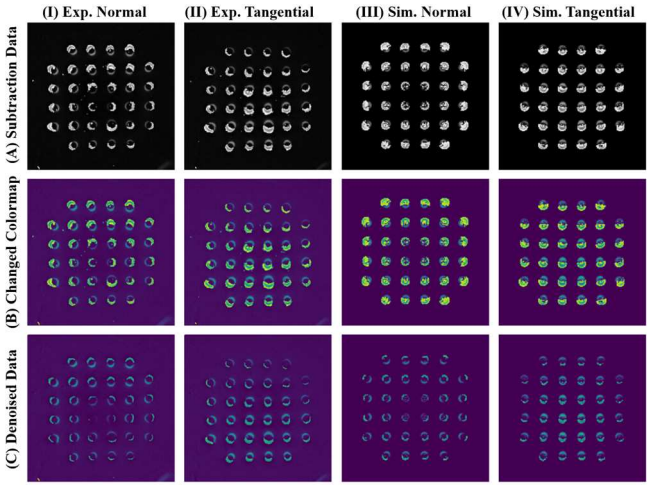

Fig. 13. Comparing the sensor behavior in simulation and experiment

V. Results

The data of the normal and tangential forces are collected in the range of up to 5 newtons for the normal axis and tangential forces up to slip. The sample output image of the sensor is shown in Fig. 12. Similar to the simulation stage, the deformation might not be evident while normal and tangential forces are applied to the compliance. Therefore, similar subtraction data were obtained from the raw images.

A. Experimental vs. Simulation

Fig. 13 compares the result of the simulation stage with the output image of the fabricated sensor. It is observed that the two datasets greatly match each other both in normal force and tangential force applications. In the experimental force–application scenario, slight eccentricity is seen which is due to the bending of the force-applying block.

B. Force Estimation

CNN model with the same structure as the simulation stage is employed for estimating normal and tangential forces, except the target size is changed from two to three. Half of the data is used as the training dataset, and the remaining half is considered as the validation and test data. Subsets of data with the same normal levels is grouped together; that being said, half of the test cycles were used for the training.

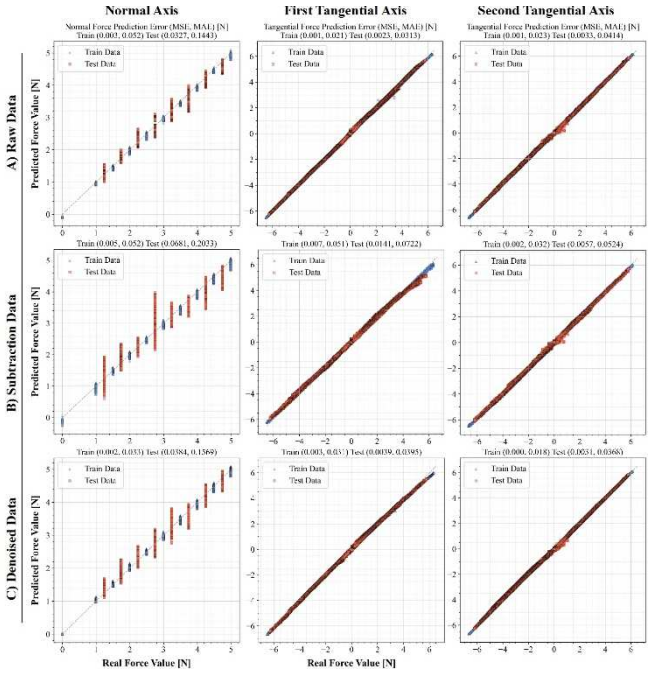

Fig. 14. Multi-axis force prediction performance of the CNN model

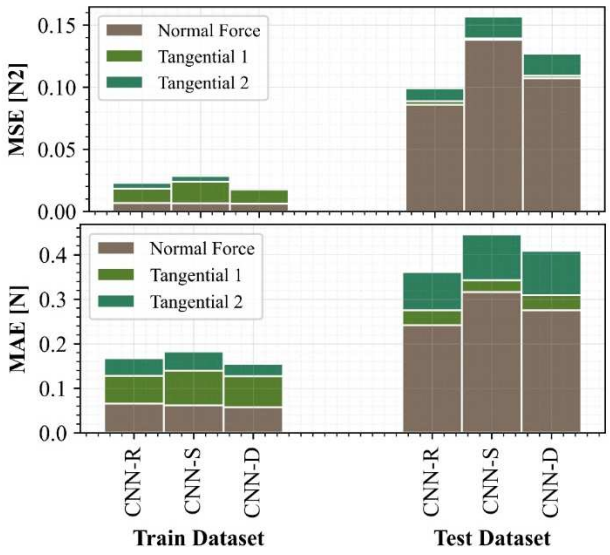

Fig. 15. Summary of the estimation error of the three models

Fig. 14 shows the prediction performance of the three CNN models trained on the raw, subtraction data, and denoised subtraction data. It is observed that the subtraction-data model's performance is weaker than the raw data and denoised-data models, especially for the normal-axis force prediction. It is also observed that the second tangential-axis force is predicted with much higher accuracy than the two other axes in all the models. To better elaborate on the performance of the sensor, Fig. 15 is presented showing the overall MSE and MAE for the test and train datasets. It is shown that the model trained on the raw images performed better on the normal-axis force estimation.

VI. Conclusion

Simulation, design, fabrication, testing, and validation of a vision-based tactile sensor were investigated in this paper. The proposed simulation framework can be utilized to estimate the performance of the sensor before the fabrication stage. CNN models were used to estimate the normal and tangential forces using the image data of both simulation and experiment. The subtraction dataset and denoised dataset were generated to be fed into the CNN models. Models trained on denoised data showed acceptable performance compared to the two other datasets while having much less computational load. Finally, the prototyped sensor could measure normal forces up to 5 N and tangential forces up to slip. The prediction MSE of the three experimental datasets showed a maximum of 0.681 N, 0.0141 N, and 0.0104 N for the estimation of the normal force and two tangential forces.

References

[1] R. S. Dahiya, G. Metta, M. Valle, and G. Sandini, "Tactile Sensing—From Humans to Humanoids," IEEE Trans. Robot., vol. 26, no. 1, pp. 1–20, Feb. 2010, doi: 10.1109/TRO.2009.2033627.

[2] Yousef, Hanna, Mehdi Boukallel, and Kaspar Althoefer. "Tactile sensing for dexterous in-hand manipulation in robotics—A review." Sensors and Actuators A: physical 167.2 (2011): 171-187.

[3] A. Shashank, M. I. Tiwana, S. J. Redmond and N. H. Lovell, "Design, simulation and fabrication of a low cost capacitive tactile shear sensor for a robotic hand," 2009 Annual International Conference of the IEEE Engineering in Medicine and Biology Society, Minneapolis, MN, USA, 2009, pp. 4132-4135, doi: 10.1109/IEMBS.2009.5332724.

[4] G. Canepa, R. Petrigliano, M. Campanella and D. De Rossi, "Detection of incipient object slippage by skin-like sensing and neural network processing," in IEEE Transactions on Systems, Man, and Cybernetics, Part B (Cybernetics), vol. 28, no. 3, pp. 348-356, June 1998, doi: 10.1109/3477.678629.

[5] M. Rabbani, M. Amin Mirzaee, M. Robati and A. Sadighi, "Design and Fabrication of a Soft Magnetic Tactile Sensor," 2022 10th RSI International Conference on Robotics and Mechatronics (ICRoM), Tehran, Iran, Islamic Republic of, 2022, pp. 491-496, doi: 10.1109/ICRoM57054.2022.10025333.

[6] M. Culjat, C. King, M. Franco, J. Bisley, W. Grundfest, and E. Dutson, "Pneumatic balloon actuators for tactile feedback in robotic surgery," Ind. Robot An Int. J., vol. 35, no. 5, pp. 449–455, Aug. 2008, doi: 10.1108/01439910810893617.

[7] M. Lambeta et al., "DIGIT: A Novel Design for a Low-Cost Compact High-Resolution Tactile Sensor With Application to In-Hand Manipulation," IEEE Robot. Autom. Lett., vol. 5, no. 3, Jul. 2020, doi: 10.1109/LRA.2020.2977257.

[8] W. Chen, H. Khamis, I. Birznieks, N. F. Lepora, and S. J. Redmond, "Tactile Sensors for Friction Estimation and Incipient Slip Detection—Toward Dexterous Robotic Manipulation: A Review," IEEE Sens. J., vol. 18, no. 22, pp. 9049–9064, Nov. 2018, doi: 10.1109/JSEN.2018.2868340.

[9] W. Yuan, S. Dong, and E. Adelson, "GelSight: High-Resolution Robot Tactile Sensors for Estimating Geometry and Force," Sensors, vol. 17, no. 12, p. 2762, Nov. 2017, doi: 10.3390/s17122762.

[10] K. Shimonomura, "Tactile Image Sensors Employing Camera: A Review," Sensors, vol. 19, no. 18, p. 3933, Sep. 2019, doi: 10.3390/s19183933.

[11] K. Shimonomura, H. Nakashima, and K. Nozu, "Robotic grasp control with high-resolution combined tactile and proximity sensing," in 2016 IEEE International Conference on Robotics and Automation (ICRA), May 2016, pp. 138–143, doi: 10.1109/ICRA.2016.7487126.

[12] M. OHKA, H. KOBAYASHI, J. TAKATA, and Y. MITSUYA, "An Experimental Optical Three-axis Tactile Sensor Featured with Hemispherical Surface," J. Adv. Mech. Des. Syst. Manuf., vol. 2, no. 5, pp. 860–873, 2008, doi: 10.1299/jamdsm.2.860.

[13] M. K. Johnson, F. Cole, A. Raj, and E. H. Adelson, "Microgeometry capture using an elastomeric sensor," ACM Trans. Graph., vol. 30, no. 4, pp. 1–8, Jul. 2011, doi: 10.1145/2010324.1964941.

[14] R. Li et al., "Localization and manipulation of small parts using GelSight tactile sensing," in 2014 IEEE/RSJ International Conference on Intelligent Robots and Systems, Sep. 2014, pp. 3988–3993, doi: 10.1109/IROS.2014.6943123.

[15] K. Sato, K. Kamiyama, N. Kawakami, and S. Tachi, "Finger-Shaped GelForce: Sensor for Measuring Surface Traction Fields for Robotic Hand," IEEE Trans. Haptics, vol. 3, no. 1, pp. 37–47, Jan. 2010, doi: 10.1109/TOH.2009.47.

[16] W. Yuan, R. Li, M. A. Srinivasan, and E. H. Adelson, "Measurement of shear and slip with a GelSight tactile sensor," in 2015 IEEE International Conference on Robotics and Automation (ICRA), May 2015, pp. 304–311, doi: 10.1109/ICRA.2015.7139016.

[17] K. Kamiyama, H. Kajimoto, N. Kawakami, and S. Tachi, "Evaluation of a vision-based tactile sensor," in IEEE International Conference on Robotics and Automation, 2004. Proceedings. ICRA '04. 2004, 2004, pp. 1542-1547 Vol.2, doi: 10.1109/ROBOT.2004.1308043.

[18] A. Yamaguchi and C. G. Atkeson, "Combining finger vision and optical tactile sensing: Reducing and handling errors while cutting vegetables," in 2016 IEEE-RAS 16th International Conference on Humanoid Robots (Humanoids), Nov. 2016, pp. 1045–1051, doi: 10.1109/HUMANOIDS.2016.7803400.

[19] L. Cramphorn, J. Lloyd, and N. F. Lepora, "Voronoi Features for Tactile Sensing: Direct Inference of Pressure, Shear, and Contact Locations," in 2018 IEEE International Conference on Robotics and Automation (ICRA), May 2018, pp. 2752–2757, doi: 10.1109/ICRA.2018.8460644.

[20] Y. Ito, Y. Kim, and G. Obinata, "Contact Region Estimation Based on a Vision-Based Tactile Sensor Using a Deformable Touchpad," Sensors, vol. 14, no. 4, pp. 5805–5822, Mar. 2014, doi: 10.3390/s140405805.

[21] Y. Ito, Y. Kim, and G. Obinata, "Slippage Degree Estimation by Using Vision-Based Tactile Sensor for Dexterous Handling," IFAC Proc. Vol., vol. 42, no. 16, pp. 281–286, 2009, doi: 10.3182/20090909-4-JP-2010.00049.

[22] J. W. James, N. Pestell, and N. F. Lepora, "Slip Detection With a Biomimetic Tactile Sensor," IEEE Robot. Autom. Lett., vol. 3, no. 4, pp. 3340–3346, Oct. 2018, doi: 10.1109/LRA.2018.2852797.

[23] B. Fang et al., "A Dual-Modal Vision-Based Tactile Sensor for Robotic Hand Grasping," in 2018 IEEE International Conference on Robotics and Automation (ICRA), May 2018, pp. 4740–4745, doi: 10.1109/ICRA.2018.8461007.

[24] A. Agarwal, T. Man, and W. Yuan, "Simulation of Vision-based Tactile Sensors using Physics based Rendering," in 2021 IEEE International Conference on Robotics and Automation (ICRA), May 2021, pp. 1–7, doi: 10.1109/ICRA48506.2021.9561122.

[25] Z. Si and W. Yuan, "Taxim: An Example-Based Simulation Model for GelSight Tactile Sensors," IEEE Robot. Autom. Lett., vol. 7, no. 2, pp. 2361–2368, Apr. 2022, doi: 10.1109/LRA.2022.3142412.

[26] S. V. Gohil, S. Suhail, J. Rose, T. Vella, and L. S. Nair, "Polymers and Composites for Orthopedic Applications," in Materials for Bone Disorders, Elsevier, 2017, pp. 349–403.

[27] I. D. Johnston, D. K. McCluskey, C. K. L. Tan, and M. C. Tracey, "Mechanical characterization of bulk Sylgard 184 for microfluidics and microengineering," J. Micromechanics Microengineering, vol. 24, no. 3, p. 035017, Mar. 2014, doi: 10.1088/0960-1317/24/3/035017.

[28] M. Olima, "Mechanical Characterization of Polydimethylsiloxane," 2017.

[29] R. N. Palchesko, L. Zhang, Y. Sun, and A. W. Feinberg, "Development of Polydimethylsiloxane Substrates with Tunable Elastic Modulus to Study Cell Mechanobiology in Muscle and Nerve," PLoS One, vol. 7, no. 12, p. e51499, Dec. 2012, doi: 10.1371/journal.pone.0051499.